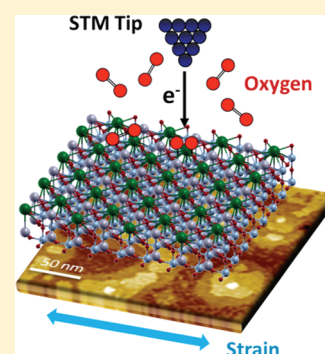


New Insights into the Strain Coupling to Surface Chemistry, Electronic Structure, and Reactivity of $\text{La}_{0.7}\text{Sr}_{0.3}\text{MnO}_3$ Helia Jalili,^{†,||} Jeong Woo Han,^{†,||} Yener Kuru,^{†,‡,§} Zhuhua Cai,^{†,‡} and Bilge Yildiz^{*,†,‡}[†]Laboratory for Electrochemical Interfaces, [‡]Department of Nuclear Science and Engineering, and [§]Department of Materials Science and Engineering, Massachusetts Institute of Technology, 77 Massachusetts Avenue, Cambridge, Massachusetts 02139, United States

S Supporting Information

ABSTRACT: Effects of strain on the surface cation chemistry and the electronic structure are important to understand and control for attaining fast oxygen reduction kinetics on transition-metal oxides. Here we demonstrate and mechanistically interpret the strain coupling to Sr segregation, oxygen vacancy formation, and electronic structure on the surface of $\text{La}_{0.7}\text{Sr}_{0.3}\text{MnO}_3$ (LSM) thin films as a model system. Our experimental results from X-ray photoelectron spectroscopy and scanning tunneling spectroscopy are discussed in light of our first principles-based simulations. A stronger Sr enrichment tendency and a more facile oxygen vacancy formation prevail for the tensile-strained LSM surface. At 500 °C in 10^{-3} mbar oxygen, both LSM film surfaces exhibit a metallic-like tunneling conductance, with a higher density of electronic states near the Fermi level on the tensile-strained LSM surface, contrary to the behavior at room temperature. Our findings illustrate the potential role and mechanism of lattice strain in tuning the reactivity of perovskite transition-metal oxides with oxygen in solid oxide fuel cell cathodes.

SECTION: Surfaces, Interfaces, Catalysis

The relation of surface cation chemistry and surface electronic structure to oxygen reduction reaction (ORR) kinetics remains an outstanding question to this day in the search for highly active cathodes for solid oxide fuel cells (SOFCs). While traditionally perovskite-type transition-metal oxides have been extensively investigated as SOFC cathodes,^{1,2} more recent studies highlight the potential of layered oxide cathodes.^{3–5} On the surface of the perovskite-structured $\text{La}_{1-x}\text{Sr}_x\text{MnO}_3$, a widely used and studied SOFC cathode material,^{1,2,6–8} the fractional presence of constituent cations can deviate from the nominal bulk stoichiometry significantly^{9–13} because of an enrichment of Sr or La cations on the surface. It has been possible to control the bulk magnetic and electronic properties of perovskite thin films by manipulating their lattice parameters with different growth conditions, hydrostatic pressure, or use of substrates with a different lattice mismatch to the films.^{14–18} Furthermore, the impact of the lattice strain on the surface electronic structure and reactivity has been long demonstrated for low-temperature noble metal electrocatalysts.^{19,20} On the other hand, the role of lattice strain on the surface cation and anion chemistry, electronic structure, and ionic transport, which all influence the ORR activity of SOFC-related oxides, is attracting its due interest only recently.

We have recently demonstrated, from first principles-based calculations, that the epitaxial strain up to a critical tensile strain value favors oxygen-vacancy formation as well as oxygen adsorption on another widely studied SOFC cathode, LaCoO_3 .²¹ Experiments validating the direct role of strain on the reactivity with oxygen and oxygen transport in SOFC materials have been

yet scarce. Sase et al. showed that the oxygen surface exchange rate at the heterointerface of $\text{La}_{0.6}\text{Sr}_{0.4}\text{CoO}_3/(\text{La},\text{Sr})_2\text{CoO}_4$ thin films is larger by three orders of magnitude compared with the single-phase cobaltite surfaces.²² A reasonable hypothesis that could explain the enhanced oxygen exchange at that interface region is the role of local strains. Studies on fluorite systems have suggested strong coupling of biaxial strain also to the oxygen ion diffusion.^{23–25}

In this Letter, we report our results, interpreted in light of our first principles-based simulations, on the strain-induced changes in the surface chemical and electronic state of $\text{La}_{0.7}\text{Sr}_{0.3}\text{MnO}_3$ (LSM) as a model system. We assessed two key parameters for reactivity with oxygen as a function of strain: (1) chemical environment on the LSM surface, in particular, the segregation of Sr cations and oxygen vacancy formation, experimentally probed with angle-resolved X-ray photoelectron spectroscopy and computationally assessed through segregation/formation energy calculations and (2) surface electronic structure, experimentally probed using scanning tunneling microscopy and spectroscopy (both at ambient and in situ at elevated temperatures) and computationally predicted with ab initio calculations.

Epitaxial 10 nm thick LSM films, grown by pulsed laser deposition²⁶ on (001) SrTiO_3 (STO) and (001) LaAlO_3 (LAO), are the model materials in this study. The XRD results (Figure S1 of

Received: February 2, 2011

Accepted: March 9, 2011

Published: March 16, 2011

the Supporting Information) indicate that both films are fully strained with the (001) out of plane orientation. The film on STO has 0.8% in-plane tensile strain, whereas the film on LAO is under -2.1% in-plane compression at room temperature. The expected strain in LSM films at the deposition temperature of $850\text{ }^{\circ}\text{C}$ is $+0.6$ and -2.3% based on the differences of the thermal expansion coefficients of LSM, STO, and LAO. The surface of LSM films grown on both substrates, hereafter denoted as LSM/LAO and LSM/STO, has well-resolved and atomically smooth terraces with different lateral sizes (Figure 1a,c). The height profiles on these terraces show that the height difference between each layer is $4.0 \pm 0.3\text{ }\text{\AA}$ (Figure 1b,d), in good agreement with the lattice parameter of the LSM ($3.88\text{ }\text{\AA}$). The overall morphology on these two substrates is similar, whereas the size of these terraces on LSM/LAO is smaller.

To assess the strain dependence of Sr content and its chemical environment on/near the surface, La 4d and Sr 3d emissions in XPS were analyzed for LSM/STO and LSM/LAO. The La 4d and Sr 3d emissions have similar kinetic energies, with a mean free path (MFP) of $20\text{ }\text{\AA}$ ^{9,10} in LSM. These spectra were

measured at two emission angles, 0 and 70° , between the surface normal and the detector position; measurements at 70° are more surface-sensitive, with a mean probing depth of $7\text{ }\text{\AA}$ from the surface. The $\text{Sr}/(\text{Sr} + \text{La})$ ratio is taken as a first measure of Sr enhancement near the surface and was quantified using the total La 4d and Sr 3d emissions normalized by their corresponding cross-sectional values from the Scofield table. The $\text{Sr}/(\text{La} + \text{Sr})$, evaluated at 70° in Figure 2a, is almost the same, 0.36 to 0.37 , on both LSM/LAO and LSM/STO and is larger than the bulk nominal value of $\text{Sr}/(\text{La} + \text{Sr}) = 0.3$. This result implies that the near-surface region of both LSM films is Sr-rich, and the total Sr fraction on the A-site ($A = \text{La}, \text{Sr}$) of LSM within the top nearly $7\text{ }\text{\AA}$ depth is the same regardless of the sign or magnitude of strain.

To obtain quantitative information about the differences in the chemical environment on LSM surfaces as a function of strain, the Sr 3d core level photoemission line shapes were analyzed. As shown in Figure 2b, the Sr 3d emission deviates from the theoretical line shape and was deconvoluted to show that it has two Sr core level binding environments on both LSM/LAO and LSM/STO. These are represented by one doublet of Sr 3d located at the lower binding energy, LBE ($132.0 \pm 0.2\text{ eV}$),²⁷ and a second doublet located at the higher binding energy, HBE ($133.4 \pm 0.2\text{ eV}$).²⁷ The LBE component has a larger contribution in the total Sr 3d emission and is attributed to the Sr cations fully coordinated within the bulk of the perovskite lattice ($\text{Sr}_{\text{lattice}}$). As the emission angle increases from 0 to 70° , the contribution of the HBE component increases, implying that the HBE binding environment is related to the Sr cations on the surface ($\text{Sr}_{\text{surface}}$) of LSM.^{10,27,28} The $\text{Sr}_{\text{surface}}$ contribution is different among the Sr 3d emissions on LSM/LAO and LSM/STO, as evident from the different line shapes of the spectra in Figure 2b. Figure 2c shows the intensity ratio of the $\text{Sr}_{\text{surface}}$ to $\text{Sr}_{\text{lattice}}$ on LSM/STO relative to that on LSM/LAO, quantified as the ratio $[(\text{Sr}_{\text{surface}}/\text{Sr}_{\text{lattice}})_{\text{LSM/STO}}]/[(\text{Sr}_{\text{surface}}/\text{Sr}_{\text{lattice}})_{\text{LSM/LAO}}]$, as a function of the emission angle. The increase in the surface Sr component with the increasing emission angle is more pronounced on LSM/STO compared with that on LSM/LAO. This ratio changes from 0.93 ± 0.05 at 0° emission to 1.23 ± 0.06 at 70° emission and shows that the $\text{Sr}_{\text{surface}}$ binding environment has a larger presence on LSM/STO. The exact nature of this HBE $\text{Sr}_{\text{surface}}$ component of the Sr 3d emission varies in different reports. Two major possibilities for the origin of the HBE component in our results are the SrO or Sr–OH phase formation on the surface^{29,30} and the under-coordinated Sr cations on the perovskite LSM surface with an AO-termination layer.^{29,31} Our STM measurements (Figure 1) do not show a significant variation in the

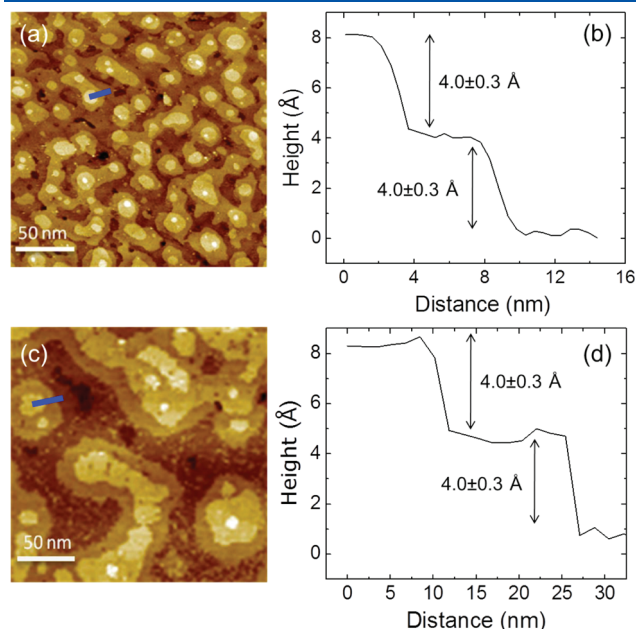


Figure 1. (a,c) Surface morphology and (b,d) height profile of the 10 nm thick (a,b) LSM/LAO and (c,d) LSM/STO films at room temperature. Blue bars in panels a and c show the position of the line profiles in panels b and d.

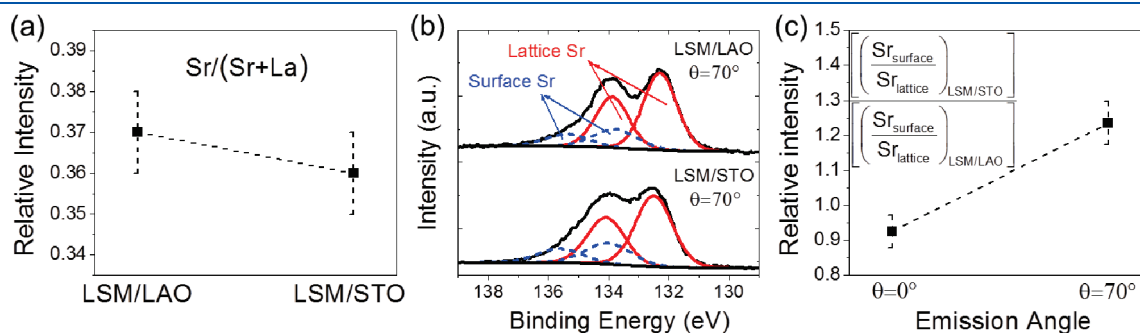


Figure 2. (a) Relative intensity of $\text{Sr}/(\text{La} + \text{Sr})$, (b) Sr 3d spectra and the two curve-fitted doublets at the high binding energy for $\text{Sr}_{\text{surface}}$ (blue/dashed line) and at the low binding energy for $\text{Sr}_{\text{lattice}}$ (red/solid line), shown for LSM/LAO and LSM/STO at 70° emission angle, and (c) the relative increase in the $\text{Sr}_{\text{surface}}$ component of the Sr 3d spectra from 0 to 70° emission angle on LSM/STO with respect to that on LSM/LAO.

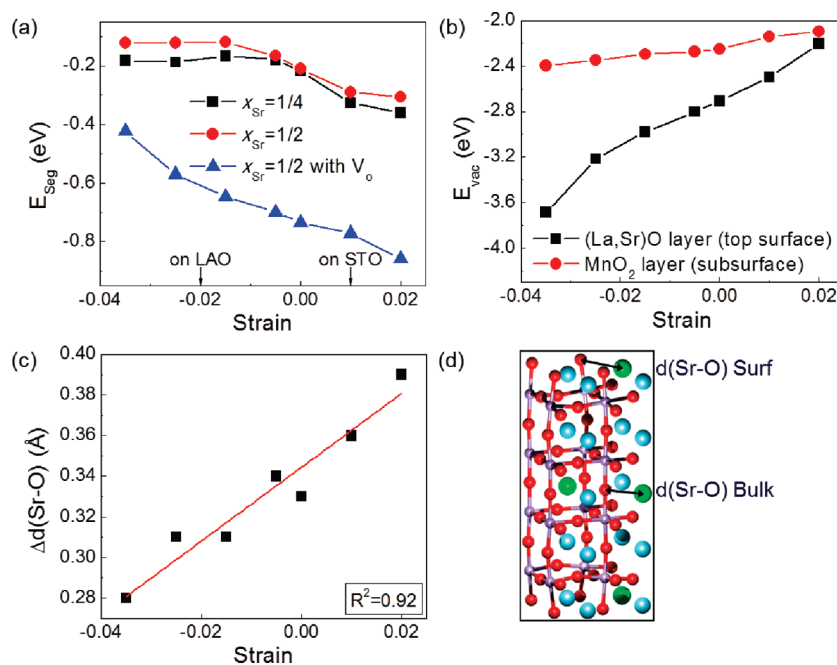


Figure 3. (a) Surface segregation energies of Sr calculated from the LSM models with $X_{\text{Sr}} = 1/4$, $1/2$, and $1/2$ including a surface oxygen vacancy under different strain states. By our definition, a more negative E_{seg} favors the Sr more strongly on the surface compared with in the bulk. (b) Oxygen vacancy formation energy as a function of strain calculated from the LSM model with $X_{\text{Sr}} = 1/2$, including one oxygen vacancy formed at the LaO layer (top surface) or at the MnO_2 layer (subsurface). By our definition, a less negative E_{vac} favors the formation of vacancy more easily on the surface. (c) Difference between the Sr–O bond length on the surface, $d(\text{Sr–O})_{\text{Surf}}$, and the Sr–O bond length in the bulk, $d(\text{Sr–O})_{\text{Bulk}}$, as a function of strain, and (d) the Sr–O bond lengths shown in the unit cell.

morphology or in the step heights that could be correlated to a discernible presence of SrO or Sr–OH surface phase. Therefore, we believe that the HBE intensity in the Sr 3d emission more likely originates from the presence of the under-coordinated Sr on the perovskite surface. Therefore, the enhanced presence of the $\text{Sr}_{\text{surface}}$ on LSM/STO suggests a further enrichment of surface Sr driven by the tensile strain state of the LSM film. However, the relative changes in $\text{Sr}_{\text{surface}}$ constitutes only about 4 to 5% difference within the total Sr 3d, which is beyond the resolution of the Sr/(Sr + La) quantification in Figure 2a.

We interpret the above result in light of our first principles-based calculations (in the framework of density functional theory (DFT)) of Sr segregation energy, E_{seg} , and vacancy formation energy, E_{vac} , as a function of strain. We assessed two models, one with 25% ($X_{\text{Sr}} = 1/4$) and another one 50% ($X_{\text{Sr}} = 1/2$) Sr on the A site on the LSM surface, as described in Figure S4 in the Supporting Information. We included the role of surface oxygen vacancies in the evaluation of E_{seg} using the $X_{\text{Sr}} = 1/2$ model. From the results shown in Figure 3a, we first note that Sr favors to segregate to the surface regardless of the amount and sign of strain from -3.5 to $+2\%$. If an element's atomic size is larger, its cohesive energy is less than that of the other constituents, or both, then it segregates more easily to the surface.³² Here the ionic radius of Sr (1.12 \AA) is larger than that of La (1.06 \AA), and the surface tension of Sr (0.29 J/m^2), which is representative of its cohesive energy, is less than that of La (0.74 J/m^2).³³ In the range of strain values assessed here, the surface of the $X_{\text{Sr}} = 1/4$ model (black curve) shows the stronger tendency to enrich Sr compared with the $X_{\text{Sr}} = 1/2$ model (red curve). Steric hindrance effects between the dopants allow them to segregate more to the surfaces with low concentrations of Sr than with high concentrations.³⁴ Furthermore, surface oxygen vacancy induces

Sr surface enrichment more strongly.^{12,35} More importantly, for all three cases shown in Figure 3a, we predict that Sr segregation tendency increases as the strain increases from compressive (-3.5%) to tensile (up to 2%). As shown in Figure 3b, oxygen vacancy formation also becomes more facile in the same strain range, potentially serving as an additional driving force for Sr enrichment. The oxygen vacancy formation is more favorable at the subsurface (MnO_2 layer) than on the top surface ((La,Sr)O layer), consistent with prior reports.³⁶ The strain response is qualitatively similar for both the top surface and the subsurface layer and favors easier oxygen vacancy formation as the strain increases from compressive (-3.5%) to tensile (up to 2%). For explaining the increasing tendency of Sr enrichment with strain, we take the space change around a Sr atom as the key measure. Figure 3c shows the difference between the Sr–O bond length on the surface and the Sr–O bond length in the bulk as a function of strain, obtained from the LSM model with $X_{\text{Sr}} = 1/4$ (Figure 3d). As the strain increases from compressive to tensile, the Sr–O bond length on the LSM surface is stretched relatively more than that in the bulk. This creates relatively more space on the surface, as shown by the increase in $\Delta d(\text{Sr–O})$. Relatively larger available space may enable easier substitution of Sr on the surface and thus lower the segregation energy. These first principles-based calculations qualitatively support and explain our experimental observations in Figure 2, favoring more Sr on the surface of tensile-strained LSM/STO.

Our experimental and theoretical results are qualitatively in agreement and show that the tensile strain can facilitate Sr segregation to the surface of LSM while the compressive strain relatively suppresses this behavior. Quantitatively, however, the Sr segregation energies predicted by our DFT calculations are large and exhibit significant dependence on strain. These calculated

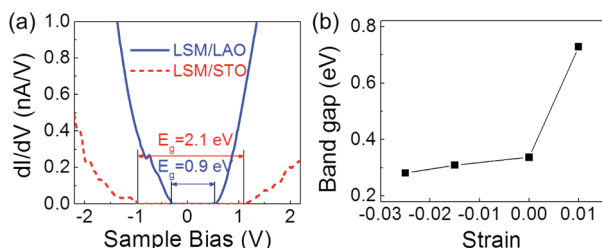


Figure 4. (a) Tunneling spectra on LSM/LAO (blue, solid line) and LSM/STO (red, dashed line), showing the energy gap, E_g , for both samples at room temperature in ultra high vacuum. (b) The band gap obtained from the DFT calculations of total density of states on LSM (001) as a function of strain.

segregation energies overestimate the total Sr enrichment as well as its strain dependence on the surface of LSM compared with our results from the angle-resolved XPS measurements. This quantitative difference is potentially due to the lack of finite temperature and kinetic effects in our models and suggests that the lattice strain alone is not the dominant driving force for Sr-related enrichment and restructuring of cations on the LSM surface.

Electronic structure is strongly coupled to the surface reactivity of the material.³⁷ Here we compare the electronic density of states using tunneling spectroscopy, probing the occupied and unoccupied states on LSM surfaces near the Fermi level both at room temperature and at an elevated temperature in oxygen. LSM surfaces at room temperature exhibited an energy gap between the occupied (negative sample bias) and unoccupied (positive sample bias) states (Figure 4a), with a smaller gap of 0.9 ± 0.2 eV on LSM/LAO compared with 2.1 ± 0.2 eV on LSM/STO. In prior tunneling studies on LSM and related perovskite thin films, differences in electronic characteristics at room temperature or below were attributed to the coexistence of paramagnetic insulating and ferromagnetic metallic regions on the surface and were related to the differences in the local Mn–O bond lengths, nanoscopic disorder,³⁸ oxidation,³⁹ and formation of oxygen vacancy defects.⁴⁰ We note that our LSM films of ~ 10 nm thickness are fully strained, and the observation of semiconducting-like energy gap at room temperature is in good agreement with previous reports on fully strained Manganite films^{39,41} and with our recent work^{13,42} on textured LSM films on zirconia substrates with a large lattice mismatch to LSM. The larger band gap found on LSM/STO compared with that on LSM/LAO may partially be related directly to the strain state differences (both magnitude and sign) on these films.

We assess the qualitative and direct relation between the epitaxial lattice strain and the electronic structure, in particular, the energy gap on LSM surface by performing density of states (DOS) calculations on LSM (001). Previous DFT calculations show that LSM is half-metallic at 0 K.^{43,44} To overcome or minimize the 0 K limitation in comparing the DOS predictions with our experimentally measured DOS at finite temperature, we need to at least represent the finite temperature magnetism of LSM⁴³ in our simulations. For this purpose, we imposed in our models the spin states of Mn ($\mu_B = 1.0$) known to be predominant at room temperature.⁴⁵ This approach allows us to model the LSM closer to its finite temperature structure⁴⁶ than the 0 K ground state. As shown in Figure S5 of the Supporting Information, the total DOS for each strain in LSM has a band gap, implying that our approach represents the band gap character of LSM at room temperature. Although our calculation results

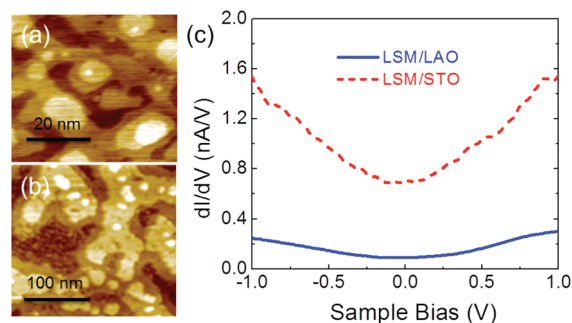


Figure 5. Surface structure on (a) LSM/LAO and (b) LSM/STO was stable at 500 °C in 10^{-3} mbar oxygen, with no evident change in morphology. (c) Tunneling spectra (dI/dV , proportional to the density of states) on LSM/LAO (blue, solid line) and LSM/STO (red, dashed line), taken at 500 °C in 10^{-3} mbar of oxygen.

do not match quantitatively our experimentally measured values of the energy gap, they qualitatively capture the trend that the band gap increases as the epitaxial strain changes from compressive to tensile (Figure 4b). It is known that DFT systematically underestimates band gaps due to the inherent lack of derivative discontinuity and delocalization errors, but the resulting qualitative trends are considered reliable.⁴⁷ The strain dependence of the energy gap that we obtained by the DFT calculations is therefore reasonably consistent with and supports our tunneling spectra results at room temperature. On the basis of our experimental and theoretical observations, we conclude that the biaxial lattice strain can induce direct changes in the surface electronic structure of LSM, determined here as the differences in the energy gap between the occupied and unoccupied states.

The picture, however, reverses for the tunneling conductance and density of states at elevated temperatures, presented in Figure 5 at 500 °C. Both of the above-mentioned films exhibit no gap between the occupied and unoccupied states (Figure 5c) at 500 °C, but a significantly larger tunneling conductance and DOS (represented by dI/dV) prevails on LSM/STO surface. The transition from the presence of an energy gap to a metallic-like electronic structure may arise from the delocalization of the charge carriers at elevated temperatures, possibly accompanied by a transition from the ferromagnetic insulator to a paramagnetic metal (for $x > 0.3$) structure⁴⁵ or due to the formation of oxygen vacancies on the surface that create defect states in the band gap.^{40,48} The thermal excitations at 500 °C are not sufficient to enable the closure of 0.9 to 2.1 eV energy gap. Moreover, and importantly for the focus of this Letter, this transition at high temperature is stronger with a larger density of states near the Fermi level for the tensile-strained LSM/STO compared with the compressively strained LSM/LAO. Taking the density of states near the Fermi level (0 V sample bias) as a measure of reactivity,³⁷ our results suggest that tensile strain state on LSM may favor electron transfer to and reactivity with oxygen at elevated temperatures in solid oxide fuel cells. We hypothesize that this difference in the electronic structure on LSM surface, directly or indirectly due to the strain state, could arise from the following two possible mechanisms. The first mechanism is associated with the formation of oxygen vacancies on the surface,³⁶ which modifies the d band structure of the neighboring transition metals and can induce states in the gap.^{49,50} More facile formation of oxygen vacancies on the tensile-strained LSM/STO, as shown in Figure 3b,

and thus, an increase in the defect states that enhances the density of states near the Fermi level is a reasonable explanation. The second mechanism is related to the possible phase changes or restructuring on LSM³⁹ as a function of temperature and Sr content.⁴⁵ The precise role of surface defects and restructuring in governing the high-temperature electronic structure and reactivity of strained LSM requires further experimental and theoretical investigation.

In summary, we demonstrated the effects of epitaxial strain on the surface cation chemistry and the surface electronic structure of LSM as a model system, both at room temperature and at elevated temperatures. A larger tendency for Sr enrichment is prevalent for the tensile-strained LSM surface, owing to the relatively larger space available for the Sr cation on the surface compared with that in the bulk with increasing tensile strain. Tensile strain also facilitates oxygen vacancy formation on LSM. While the electronic structure exhibits the presence of an energy gap between the occupied and unoccupied states at room temperature, favoring a smaller band gap for the compressively strained LSM, the picture reverses at elevated temperatures. At 500 °C in 10^{−3} mbar of oxygen, both LSM film surfaces exhibit metallic-like behavior, and the tensile-strained LSM has enhanced density of states near the Fermi level compared with the compressively strained LSM. These results illustrate the importance of lattice strain in controlling the high-temperature surface chemistry and electronic structure for oxygen reduction activity on SOFC cathodes. In-depth probing and analysis of such correlations on a broad range of materials and conditions are essential toward advancing our understanding of how the surface state, including the presence of strain, relates to the oxygen reduction activity on oxide cathodes. Integration of surface-sensitive in situ techniques and first principles-based simulations, as demonstrated here, is a necessary approach for this goal.

METHODS

Experimental Methods. X-ray diffraction (XRD) measurements were performed employing a PANalytical Expert Pro MPD diffractometer to determine the phase purity and the strain states. Scanning tunneling microscopy/spectroscopy (STM/STS) at room temperature as well as at elevated temperatures was used to investigate the surface morphology and electronic structure of the strained films. The measurements were performed in a modified ultra high vacuum (UHV) system designed by Omicron Nanotechnology, with a variable temperature scanning tunneling microscope. The chemical state of the surfaces was probed using angle-resolved X-ray photoelectron spectroscopy (XPS) using a five-channel hemispherical electron analyzer, equipped in the same chamber with the STM. CasaXPS 2.3.15 software was used to assess the spectra and calculate the relative intensity of each constituent by employing the Shirley background. The total intensity of each constituent was normalized by their corresponding cross section values from Scofield's table. We removed carbon contamination from the surfaces of the air-exposed LSM films by heating them in oxygen pressure of 5 × 10^{−5} mbar at 500 °C for at least 30 min in the UHV chamber. All STM, STS, and XPS results reported here were obtained after the cleaning process. A pyrolytic boron nitride (PBN) heater was used to evenly heat the LSM films during the cleaning process as well as during the STM experiments at high temperatures. STM measurements were performed in the constant-current mode using Pt/Ir tips, with a bias voltage of 1 to 2 V applied to the tip and a tunneling current of 200–500 pA.

Computational Method. Plane-wave DFT calculations were performed using the Vienna ab initio simulation package (VASP)⁵¹ to assess the surface Sr segregation energetics, from −3.5% (compressive) to +2% (tensile) on LSM. We employed the generalized gradient approximation (GGA) parametrized by Perdew and Wang⁵² along with the projector augmented wave (PAW) method⁵³ to describe the ionic cores. To avoid the self-interaction errors that occur in the traditional DFT for strongly correlated electronic systems, we employed the DFT+U method, with a correction parameter of $U - J = 4$ eV.⁵⁴ All calculations used a plane wave expansion cutoff of 400 eV and included spin polarization. The DFT-optimized cubic lattice constant of LSM was 3.93 Å, in good agreement with the experimental value of 3.88 Å. This bulk structure of LaMnO₃ was cleaved along the (001) plane, with the (La,Sr)O-terminated surface, to construct a surface consistent with our PLD-grown epitaxial films. Two-dimensional planar lattice strain was imposed by elongating the simulation cell in the *x* and *y* directions and relaxing the cell configuration and dimension in the *z* direction. The slab model is 15.5 Å thick and contains nine atomic symmetric layers with the middle three layers constrained in their bulk positions. The symmetric slab was chosen to avoid the fictitious dipole moment. We have chosen a (2 × 2) surface unit cell and a 4 × 4 × 1 Monkhorst-Pack *k*-point mesh, which gives a convergence of ~0.5 meV/atom. For the DOS calculations, the *k*-point mesh is increased to 8 × 8 × 1 centered at Γ using the tetrahedron method with Blöchl corrections.⁵⁵

ASSOCIATED CONTENT

S Supporting Information. X-ray diffraction patterns, scanning tunneling spectra (STS) taken on La_{0.7}Sr_{0.3}MnO₃ films grown on SrTiO₃ (STO) and LaAlO₃ (LAO), DFT model construction and description, and calculated total density of states on LSM(001) that show a change in the band gap value as a function of strain. This material is available free of charge via the Internet at <http://pubs.acs.org>.

AUTHOR INFORMATION

Corresponding Author

*E-mail: byildiz@mit.edu.

Author Contributions

^{||}These authors contributed equally to this work.

ACKNOWLEDGMENT

We thank Paul Salvador for providing the samples for this investigation, the US–DOE, Office of Fossil Energy, grant no. DE-NT0004117, and Basic Energy Sciences, grant no. DE-SC0002633 for financial support, and the National Science Foundation for computational support through the TeraGrid Advanced Support Program, grant no. TG-ASC090058.

REFERENCES

- (1) Adler, S. B. Factors Governing Oxygen Reduction in Solid Oxide Fuel Cell Cathodes. *Chem. Rev.* **2004**, *104*, 4791–4843.
- (2) Jacobson, A. J. Materials for Solid Oxide Fuel Cells. *Chem. Mater.* **2010**, *22*, 660–674.
- (3) Chronos, A.; Parfitt, D.; Kilner, J. A.; Grimes, R. W. Anisotropic Oxygen Diffusion in Tetragonal La₂NiO_{4+δ}: Molecular Dynamics Calculations. *J. Mater. Chem.* **2010**, *20*, 266–270.

- (4) Tarancón, A.; Burriel, M.; Santiso, J.; Skinner, S. J.; Kilner, J. A. Advances in Layered Oxide Cathodes for Intermediate Temperature Solid Oxide Fuel Cells. *J. Mater. Chem.* **2010**, *20*, 3799–3813.
- (5) Kushima, A.; Parfitt, D.; Chronos, A.; Yildiz, B.; Kilner, J. A.; Grimes, R. W. Interstitialcy Diffusion of Oxygen in Tetragonal $\text{La}_2\text{CoO}_{4+\delta}$. *Phys. Chem. Chem. Phys.* **2011**, *13*, 2242–2249.
- (6) Choi, Y.; Lynch, M. E.; Lin, M. C.; Liu, M. Prediction of O_2 Dissociation Kinetics on LaMnO_3 -Based Cathode Materials for Solid Oxide Fuel Cells. *J. Phys. Chem. C* **2009**, *113*, 7290–7297.
- (7) Mastrov, Y. A.; Merkle, R.; Heifets, E.; Kotomin, E. A.; Maier, J. Pathways for Oxygen Incorporation in Mixed Conducting Perovskites: A DFT-Based Mechanistic Analysis for $(\text{La}, \text{Sr})\text{MnO}_{3-\delta}$. *J. Phys. Chem. C* **2010**, *114*, 3017–3027.
- (8) Co, A. C.; Birss, V. I. Mechanistic Analysis of the Oxygen Reduction Reaction at $(\text{La}, \text{Sr})\text{MnO}_3$ Cathodes in Solid Oxide Fuel Cells. *J. Phys. Chem. B* **2006**, *110*, 11299–11309.
- (9) Dulli, H.; Dowben, P. A.; Liou, S. H.; Plummer, E. W. Surface Segregation and Restructuring of Colossal-Magnetoresistant Manganese Perovskites $\text{La}_{0.65}\text{Sr}_{0.35}\text{MnO}_3$. *Phys. Rev. B* **2000**, *62*, R14629–R14632.
- (10) Bertacco, R.; Contour, J. P.; Barthélemy, A.; Olivier, J. Evidence for Strontium Segregation in $\text{La}_{0.7}\text{Sr}_{0.3}\text{MnO}_3$ Thin Films Grown by Pulse Laser Deposition: Consequences for Tunneling Junctions. *Surf. Sci.* **2002**, *511*, 366–372.
- (11) Wu, Q.-H.; Liu, M.; Jaegermann, W. X-ray Photoelectron Spectroscopy of $\text{La}_{0.5}\text{Sr}_{0.5}\text{MnO}_3$. *Mater. Lett.* **2005**, *59*, 1980–1983.
- (12) Fister, T. T.; Fong, D. D.; Eastman, J. A.; Baldo, P. M.; Highland, M. J.; Fuoss, P. H.; Balasubramanian, K. R.; Meador, J. C.; Salvador, P. A. In Situ Characterization of Strontium Surface Segregation in Epitaxial $\text{La}_{0.7}\text{Sr}_{0.3}\text{MnO}_3$ Thin Films as a Function of Oxygen Partial Pressure. *Appl. Phys. Lett.* **2008**, *93*, 151904/1–151904/3.
- (13) Katsiev, K.; Yildiz, B.; Balasubramanian, K.; Salvador, P. A. Electron Tunneling Characteristics on $\text{La}_{0.7}\text{Sr}_{0.3}\text{MnO}_3$ Thin-Film Surfaces at High Temperature. *Appl. Phys. Lett.* **2009**, *95*, 092106/1–092106/3.
- (14) Daoudi, K.; Tsuchiya, T.; Yamaguchi, I.; Manabe, T.; Mizuta, S.; Kumagai, T. Microstructural and Electrical Properties of $\text{La}_{0.7}\text{Ca}_{0.3}\text{MnO}_3$ Thin Films Grown on SrTiO_3 and LaAlO_3 Substrates Using Metal-Organic Deposition. *J. Appl. Phys.* **2005**, *98*, 013507/1–013507/6.
- (15) Gebhardt, U.; Kasper, N. V.; Vigliante, A.; Wochner, P.; Dosch, H.; Razavi, F. S.; Habermeyer, H. U. Formation and Thickness Evolution of Periodic Twin Domains in Manganite Films Grown on $\text{SrTiO}_3(001)$ Substrates. *Phys. Rev. Lett.* **2007**, *98*, 096101/1–096101/4.
- (16) Razavi, F. S.; Rao, G. V. S.; Jalili, H.; Habermeyer, H. U. Pressure Induced Phase Transition in Periodic Microtwinning Thin Film of $\text{La}_{0.88}\text{Sr}_{0.12}\text{MnO}_3$. *Appl. Phys. Lett.* **2006**, *88*, 174103/1–174103/3.
- (17) Ding, Y.; Haskel, D.; Tseng, Y.-C.; Kaneshta, E.; van Veenendaal, M.; Mitchell, J. F.; Sinogeikin, S. V.; Prakapenka, V.; Mao, H.-K. Pressure-Induced Magnetic Transition in Manganite ($\text{La}_{0.75}\text{Ca}_{0.25}\text{MnO}_3$). *Phys. Rev. Lett.* **2009**, *102*, 237201/1–237201/4.
- (18) Rata, A. D.; Herklotz, A.; Nenkov, K.; Schultz, L.; Dörr, K. Strain-Induced Insulator State and Giant Gauge Factor of $\text{La}_{0.7}\text{Sr}_{0.3}\text{CoO}_3$ Films. *Phys. Rev. Lett.* **2008**, *100*, 076401/1–076401/4.
- (19) Mavrikakis, M.; Hammer, B.; Nørskov, J. K. Effect of Strain on the Reactivity of Metal Surfaces. *Phys. Rev. Lett.* **1998**, *81*, 2819–2822.
- (20) Strasser, P.; Koh, S.; Anniyev, T.; Greeley, J.; More, K.; Yu, C.; Liu, Z.; Kaya, S.; Nordlund, D.; Ogasawara, H.; et al. Lattice-Strain Control of the Activity in Dealloyed Core–Shell Fuel Cell Catalysts. *Nat. Chem.* **2010**, *2*, 454–460.
- (21) Kushima, A.; Yip, S.; Yildiz, B. Competing Strain Effects in Reactivity of LaCoO_3 with Oxygen. *Phys. Rev. B* **2010**, *82*, 115435/1–115435/6.
- (22) Sase, M.; Yashiro, K.; Sato, K.; Mizusaki, J.; Kawada, T.; Sakai, N.; Yamaji, K.; Horita, T.; Yokokawa, H. Enhancement of Oxygen Exchange at the Hetero Interface of $(\text{La}, \text{Sr})\text{CoO}_3/(\text{La}, \text{Sr})_2\text{CoO}_4$ in Composite Ceramics. *Solid State Ionics* **2008**, *178*, 1843–1852.
- (23) Garcia-Barriocanal, J.; Rivera-Calzada, A.; Varela, M.; Sefrioui, Z.; Iborra, E.; Leon, C.; Pennycuik, S. J.; Santamaria, J. Colossal Ionic Conductivity at Interfaces of Epitaxial $\text{ZrO}_2\text{:Y}_2\text{O}_3/\text{SrTiO}_3$ Heterostructures. *Science* **2008**, *321*, 676–680.
- (24) Kushima, A.; Yildiz, B. Oxygen Ion Diffusivity in Strained Yttria Stabilized Zirconia: Where is the Fastest Strain?. *J. Mater. Chem.* **2010**, *20*, 4809–4819.
- (25) Schichtel, N.; Korte, C.; Hesse, D.; Janek, J. Elastic Strain at Interfaces and its Influence on Ionic Conductivity in Nanoscaled Solid Electrolyte Thin Films-Theoretical Considerations and Experimental Studies. *Phys. Chem. Chem. Phys.* **2009**, *11*, 3043–3048.
- (26) Balasubramanian, K. R.; Havelia, S.; Salvador, P. A.; Zheng, H.; Mitchell, J. F. Epitaxial Stabilization and Structural Properties of REMnO_3 ($\text{RE} = \text{Dy}, \text{Gd}, \text{Sm}$) Compounds in a Layered, Hexagonal ABO_3 Structure. *Appl. Phys. Lett.* **2007**, *91*, 232901/1–232901/3.
- (27) van der Heide, P. A. W. Systematic X-ray Photoelectron Spectroscopic Study of $\text{La}_{1-x}\text{Sr}_x$ -based Perovskite-Type Oxides. *Surf. Interface Anal.* **2002**, *33*, 414–425.
- (28) Vovk, G.; Chen, X.; Mims, C. A. In Situ XPS Studies of Perovskite Oxide Surfaces under Electrochemical Polarization. *J. Phys. Chem. B* **2005**, *109*, 2445–2454.
- (29) van der Heide, P. A. W.; Rabalais, J. W. Photoelectron Spectroscopic Study of the Temperature-Dependent Termination of the $\text{LaAlO}_3(100)$ Surface. *Chem. Phys. Lett.* **1998**, *297*, 350–356.
- (30) Dupin, J.-C.; Gonbeau, D.; Vinatier, P.; Levasseur, A. Systematic XPS Studies of Metal Oxides, Hydroxides and Peroxides. *Phys. Chem. Chem. Phys.* **2000**, *2*, 1319–1324.
- (31) Hudson, L. T.; Kurtz, R. L.; Robey, S. W.; Temple, D.; Stockbauer, R. L. Surface Core-Level Shifts of Barium Observed in Photoemission of Vacuum-Fractured $\text{BaTiO}_3(100)$. *Phys. Rev. B* **1993**, *47*, 10832–10838.
- (32) Han, J. W.; Kitchin, J. R.; Sholl, D. S. Step Decoration of Chiral Metal Surfaces. *J. Chem. Phys.* **2009**, *130*, 124710/1–124710/8.
- (33) Lu, H. M.; Jiang, Q. Surface Tension and Its Temperature Coefficient for Liquid Metals. *J. Phys. Chem. B* **2005**, *109*, 15463–15468.
- (34) Sayle, T. X. T.; Parker, S. C.; Catlow, C. R. A. Surface Segregation of Metal Ions in Cerium Dioxide. *J. Phys. Chem.* **1994**, *98*, 13625–13630.
- (35) Caillol, N.; Pijolat, M.; Siebert, E. Investigation of Chemisorbed Oxygen, Surface Segregation and Effect of Post-Treatments on $\text{La}_{0.8}\text{Sr}_{0.2}\text{MnO}_3$ Powder and Screen-Printed Layers for Solid Oxide Fuel Cell Cathodes. *Appl. Surf. Sci.* **2007**, *253*, 4641–4648.
- (36) Lee, Y.-L.; Morgan, D. Prediction of Surface Oxygen Vacancy Concentrations of $(\text{La}_{1-x}\text{Sr}_x)\text{MnO}_3$. *ECS Trans* **2009**, *25*, 2769–2774.
- (37) Gross, A. *Theoretical Surface Science: A Microscopic Perspective*, 2nd ed.; Springer-Verlag: Berlin, 2009.
- (38) Bibes, M.; Balcells, L.; Valencia, S.; Fontcuberta, J.; Wojcik, M.; Jedryka, E.; Nadolski, S. Nanoscale Multiphase Separation at $\text{La}_{2/3}\text{Ca}_{1/3}\text{MnO}_3/\text{SrTiO}_3$ Interfaces. *Phys. Rev. Lett.* **2001**, *87*, 067210/1–067210/4.
- (39) Fuchigami, K.; Gai, Z.; Ward, T. Z.; Yin, L. F.; Snijders, P. C.; Plummer, E. W.; Shen, J. Tunable Metallicity of the $\text{La}_{5/8}\text{Ca}_{3/8}\text{MnO}_3$ (001) Surface by an Oxygen Overlayer. *Phys. Rev. Lett.* **2009**, *102*, 066104/1–066104/4.
- (40) Szot, K.; Speier, W.; Carius, R.; Zastrow, U.; Beyer, W. Localized Metallic Conductivity and Self-Healing during Thermal Reduction of SrTiO_3 . *Phys. Rev. Lett.* **2002**, *88*, 075508/1–075508/4.
- (41) Okawa, N.; Tanaka, H.; Akiyama, R.; Matsumoto, T.; Kawai, T. Effects of Film Thickness on Surface Flatness and Physical Properties in $\text{La}_{1-x}\text{Sr}_x\text{MnO}_3$ Thin Films Investigated by Scanning Tunneling Microscopy. *Solid State Commun.* **2000**, *114*, 601–605.
- (42) Katsiev, K.; Yildiz, B.; Kavaipatti, B.; Salvador, P. Correlations of Electronic and Chemical State on $\text{La}_{0.7}\text{Sr}_{0.3}\text{MnO}_3$ Dense Thin-Film Cathode Surfaces. *ECS Trans* **2009**, *25*, 2309–2318.
- (43) Pruneda, J. M.; Ferrari, V.; Rurali, R.; Littlewood, P. B.; Spaldin, N. A.; Artacho, E. Ferrodistorive Instability at the (001) Surface of Half-Metallic Manganites. *Phys. Rev. Lett.* **2007**, *99*, 226101/1–226101/4.
- (44) Ma, C.; Yang, Z. Q.; Picozzi, S. Ab Initio Electronic and Magnetic Structure in $\text{La}_{0.66}\text{Sr}_{0.33}\text{MnO}_3$: Strain and Correlation Effects. *J. Phys.: Condens. Matter* **2006**, *18*, 7717–7728.

(45) Urushibara, A.; Moritomo, Y.; Arima, T.; Asamitsu, A.; Kido, G.; Tokura, Y. Insulator-Metal Transition and Giant Magnetoresistance in $\text{La}_{1-x}\text{Sr}_x\text{MnO}_3$. *Phys. Rev. B* **1995**, *51*, 14103–14109.

(46) Pandey, S. K.; Kumar, A.; Patil, S.; Medicherla, V. R. R.; Singh, R. S.; Maiti, K.; Prabhakaran, D.; Boothroyd, A. T.; Pimpale, A. V. Investigation of the Spin State of Co in LaCoO_3 at Room Temperature: Ab Initio Calculations and High-Resolution Photoemission Spectroscopy of Single Crystals. *Phys. Rev. B* **2008**, *77*, 045123/1–045123/7.

(47) Sholl, D. S.; Steckel, J. A. *Density Functional Theory: A Practical Introduction*; John Wiley & Sons, Inc.: Hoboken, NJ, 2009.

(48) Diebold, U.; Li, S.-C.; Schmid, M. Oxide Surface Science. *Annu. Rev. Phys. Chem.* **2010**, *61*, 129–148.

(49) Ganduglia-Pirovano, M. V.; Hofmann, A.; Sauer, J. Oxygen Vacancies in Transition Metal and Rare Earth Oxides: Current State of Understanding and Remaining Challenges. *Surf. Sci. Rep.* **2007**, *62*, 219–270.

(50) Kim, Y. S.; Kim, J.; Moon, S. J.; Choi, W. S.; Chang, Y. J.; Yoon, J. G.; Yu, J.; Chung, J. S.; Noh, T. W. Localized Electronic States Induced by Defects and Possible Origin of Ferroelectricity in Strontium Titanate Thin Films. *Appl. Phys. Lett.* **2009**, *94*, 202906/1–202906/3.

(51) Kresse, G.; Furthmüller, J. Efficient Iterative Schemes for Ab Initio Total-Energy Calculations Using a Plane-Wave Basis Set. *Phys. Rev. B* **1996**, *54*, 11169–11186.

(52) Perdew, J. P.; Chevary, J. A.; Vosko, S. H.; Jackson, K. A.; Pederson, M. R.; Singh, D. J.; Fiolhais, C. Atoms, Molecules, Solids, and Surfaces: Applications of the Generalized Gradient Approximation for Exchange and Correlation. *Phys. Rev. B* **1992**, *46*, 6671–6687.

(53) Blöchl, P. E. Projector Augmented-Wave Method. *Phys. Rev. B* **1994**, *50*, 17953–17979.

(54) Wang, L.; Maxisch, T.; Ceder, G. Oxidation Energies of Transition Metal Oxides within the GGA+U Framework. *Phys. Rev. B* **2006**, *73*, 195107/1–195107/6.

(55) Blöchl, P. E.; Jepsen, O.; Andersen, O. K. Improved Tetrahedron Method for Brillouin-Zone Integrations. *Phys. Rev. B* **1994**, *49*, 16223–16233.